Momentum and heat transfer in turbulent channels with drag-increasing riblets

Journal of Physics: Conference Series **3173** (2026) 012004 doi:10.1088/1742-6596/3173/1/012004

Momentum and heat transfer in turbulent channels with drag-increasing riblets

S. Cipelli[1], N. Rapp[1], B. Frohnapfel[1] and D. Gatti[1]

[1]Institute of Fluid Mechanics, Karlsruhe Institute of Technology (KIT), Kaiserstraße 10, 76131 Karlsruhe, Germany

E-mail: stefano.cipelli@kit.edu

Abstract. We perform Direct Numerical Simulations (DNS) of turbulent channel flows with riblets in the drag-increasing regime. The objective is to investigate whether sufficiently large riblets diverge from the typical k-roughness regime and to evaluate whether some geometries, compared to a smooth channel, enhance heat transfer more than momentum transfer. To obtain different riblets viscous sizes, we vary the riblet size in outer units and adjust the Reynolds number. The results for friction are consistent with experimental findings from von Deyn et al. [17] for the same trapezoidal riblets geometry and indicate that these geometries deviate from the k-roughness regime. Furthermore, all tested geometries can improve the Reynolds analogy factor relative to a smooth channel by $\approx 1-2\%$.

1 Introduction

Riblets are known for their ability to reduce drag when their viscous size is small relative to the turbulent buffer layer. Over the past 40 years, various riblet configurations have been extensively studied through experiments ([2, 17]) and simulations ([5, 3]), all demonstrating that performance strongly depends on the cross-sectional shape. As theorized by Luchini [10], drag reduction originates from a positive offset between the virtual origins perceived by longitudinal and transverse Stokes flows. This effect dominates in the viscous regime, where drag reduction aligns closely with Stokes flow predictions. However, as riblets grow larger and interact with the buffer layer, drag-increasing phenomena emerge ([4, 12]).

From this point onward, riblet size will be represented by the square root of the groove cross-sectional area (l_g^+), which more universally characterises the riblets' roughness function compared to other geometrical quantities [4].

The drag-increasing regime has received less attention due to its perceived lack of practical interest. Recent experiments by von Deyn et al. [17], however, revealed that ribbed surfaces deviate from the expected k-roughness behavior. Instead of a logarithmic increase of the roughness function ΔU^+ with roughness size, they exhibit a peak around 50 viscous units followed by a plateau. This behavior was attributed to riblet geometries lacking pressure drag and the wall being perceived as piecewise smooth by turbulence. Consequently, beyond a certain size, further increases in riblets' viscous size minimally affect drag, with residual differences with respect to a smooth wall attributed to corner-induced effects. Other experiments by Rowin et al. [16] for triangular riblets didn't show the same behavior, but the l_g^+ range was limited to values smaller than 110 wall units, a size at which also von Deyn et al. [17] didn't notice deviations from the k-roughness behavior for triangular geometries.

Regarding thermal efficiency, Rouhi et al. [15] showed that large riblets can enhance the Reynolds analogy coefficient, with Stanton number increases outpacing those of the friction coefficient. This effect is often linked to Kelvin-Helmholtz rollers in the near-wall region, whereas secondary motions typically reduce efficiency.

This study aims to investigate riblet performance in the drag-increasing regime, evaluating heat and momentum transfer capabilities and comparing the results with the aforementioned studies.

2 Method

The DNS code by Luchini et al. [11] solves the incompressible Navier-Stokes equations on a staggered grid using second-order finite differences in all directions. The momentum equation is advanced in time via a fractional time-stepping method with a third-order Runge–Kutta scheme, adapting the timestep to achieve a constant CFL number. The time-advancement is explicit, except for the treatment of the immersed boundary terms, and the Poisson equation for pressure is solved through an iterative successive over-relaxation algorithm applied to a Gauss-Seidel red-black iteration.

We perform DNS of turbulent channel flows in a full-domain configuration with two walls, spanning $(2\pi,\, \pi,\, 2)\,\delta$ in the longitudinal (x), spanwise (y), and wall-normal (z) directions, where δ is the half-channel height. The grid is cartesian and the wall is represented via an innovative immersed boundary approach, which employs the local steady Stokes solution of the flow around the tip geometry to improve the accuracy of the simulation without having to recur to extremely fine grid resolutions ([7]). The resolution parameters are the following: $\Delta x^+ = 6.0$, $\Delta y^+ = 1.0 \div 3.0$, and $\Delta z^+ = 0.8 \div 4.0$. In the spanwise direction, the grid is finest at the tips, while it is coarser in correspondence of the valleys. In the wall-normal direction the grid spacing is almost uniform until the riblet tips, and it increases with a natural stretching ([14]) towards half channel. All details about the simulation set-up parameters are reported in Table 1.

Ribbed channels with symmetric straight riblets on both walls are compared to smooth counterparts at equivalent Reynolds numbers. The wall position is defined such that the smooth-wall reference lies at a distance of $h_{\parallel}$ below the riblet tips, where $h_{\parallel}$ is the longitudinal protrusion height ([10]) for the given riblet geometry. This alignment ensures valid comparisons across different Reynolds numbers, as $h_{\parallel}$ matches the position where a smooth wall would yield the same laminar profile as the ribbed one.

We simulate the incompressible Navier-Stokes equations along with a transport equation for a passive scalar (temperature) with unitary Prandtl number ($Pr = 1$). Both flow and scalar fields are treated similarly: the fluid is driven by a constant pressure gradient, and the temperature is subject to a uniform volumetric heating. Boundary conditions are periodic in the x and y directions, with no-slip and zero-temperature conditions at the walls. Simulations are run for approximately 100 large-eddy-turnover time units.

l_g	l_g^+	Re_τ	n_x	n_y	n_z	t_{let}
0.053	20	375	408	816	291	100.6
0.12	30	250	272	556	271	110.2
0.24	50	208	226	430	279	94.6
0.12	50	417	452	922	379	98.5
0.24	100	417	452	860	561	94.5
0.12	100	833	904	1860	473	93.8
0.24	150	625	678	1488	417	109.4
0.24	200	833	904	1968	485	86.8

Table 1: Design parameters for the performed simulations. l_g and l_g^+ represent the riblet size in outer and viscous units, in terms of square root of the groove cross section. Re_τ is the friction Reynolds number. n_x, n_y and n_z represent the number of grid points in the streamwise, spanwise and wall-normal directions, while t_{let} represents the simulation duration in large-eddy-turnover time units.

3 Results and Discussion

The simulated geometries share the same cross-sectional shape: trapezoidal riblets with a 60° tip angle and a height-to-spacing ratio (k/s) of approximately 0.38. Their outer unit sizes, based on the square root of the groove cross-section, are $l_g = 0.053$, 0.12, and 0.24, tested at varying Reynolds numbers to span a broad range of l_g^+ values between 20 and 200. Details of geometric parameters and results are

l_g	l_g^+	Re_τ	ΔC_f %	ΔC_h%	ΔU^+	$\Delta\Theta^+$	RA/RA_0
0.053	20	375	3.6	4.4	0.34	0.48	1.008
0.12	30	250	16.7	18.4	1.42	1.63	1.014
0.24	50	208	34.8	37.0	2.88	3.11	1.017
0.12	50	417	33.3	37.0	2.79	3.15	1.028
0.24	100	417	24.5	26.3	2.73	2.77	1.014
0.12	100	833	23.6	28.1	2.90	3.11	1.037
0.24	150	625	21.4	23.4	2.71	2.69	1.017
0.24	200	833	21.2	23.6	2.59	2.66	1.020

Table 2: Simulations results. ΔC_f and ΔC_h denote the percentage differences in the friction coefficient and Stanton number compared to a smooth channel, while ΔU^+ and $\Delta\Theta^+$ indicate shifts in the logarithmic layer of the velocity and scalar profiles. RA/RA_0 represents the ratio of the Reynolds analogy factor of the ribbed channel to that of a smooth channel.

presented in Table 2.

The presence of large riblets implies that the assumption of a smooth-wall-like turbulence is not fully applicable ([8]), as the turbulent shear stress profiles of ribbed and smooth channels differ significantly in the near-wall region. For this reason, the evaluation of ΔU^+ and $\Delta\Theta^+$ is not straightforward. To compare the present results with those from von Deyn et al. [17], we calculate the shifts in the mean velocity and temperature profiles using the friction coefficient and Stanton number, as per Equation 4.8 from Gatti and Quadrio [6]. The mentioned formula, while being exact for smooth channels, is not extremely accurate for ribbed geometries, as the riblet-to-channel height ratio (k/δ) is not infinitesimal. However, it allows for comparison with the experimental results, and supports the observed agreement between the datasets. In fact, when the numerical results are compared with experimental data obtained for the same cross section (●●), all data points essentially collapse onto the experimental curve.

Another, more robust, option to estimate ΔU^+ is to actually calculate the difference in the mean velocity profile between the smooth and the ribbed channels, at matched Re_τ. ΔU^+ is calculated as an average of the difference of the profiles in the logaritmic region, under the assumption that the Reynolds numbers of the smooth and ribbed channels are identical.

While such measurements are state of the art for canonical rough surfaces, drag-reducing riblets, and for assessing the drag reduction achieved by other active control strategies, it must be noted that the virtual origin of turbulence is not straightforward to define in these cases. In the case of small riblets, the origin can be clearly identified from the wall-normal shift in the Reynolds shear stress profiles. However, for larger riblets in plus-units, a secondary peak in the $\overline{u'w'}^+$ profiles emerges within the groove region, making the definition less obvious. For this reason, in all cases we place the equivalent smooth-channel height at a distance of $h_\parallel$ from the riblet crest. Results in terms of ΔU^+ and $\Delta\Theta^+$, calculated both from the friction coefficient/Stanton number and from the mean profiles are presented respectively in Figure 1, 2.

As regards the friction roughness function, when evaluating it through the friction coefficients, the results clearly match the experimental dataset for all cases, with small differences in the large l_g^+ regime. On the other hand, when using the mean velocity profiles, a distinct peak in the ΔU^+ is not clearly visible, and the shift in the mean velocity profile is roughly constant for the cases with $l_g^+ \geq 50$. The present discrepancy between the two methods will be discussed later in the paper.

What remains clear is that the experimental trend persists: ribbed geometries do not appear to conform to the typical k-roughness regime. Results obtained at $l_g^+ = 50$, 100, using different Reynolds numbers while maintaining the same viscous-scaled riblet size, indicate that the influence of the Reynolds number on the roughness function is limited. Despite the relatively large riblets, reaching a riblet-to-channel-height ratio of up to 0.15, it seems plausible that coherent velocity fields extending into the logarithmic region have minimal impact on the evaluation of ΔU^+.

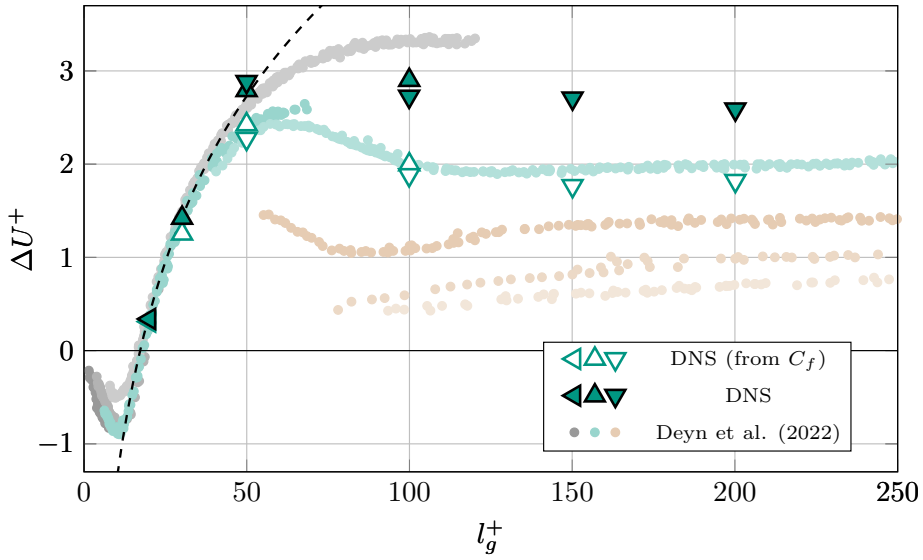

Figure 1: Comparison between the experimental data from [17] (● ● ●) and the present numerical results (◁ △ ▽, ◀ ▲ ▼) for ΔU^+. Different marker colors represent different cross-sectional shapes: grey (● ● ●) for triangular riblets, green (● ● △ ▲) for trapezoidal riblets with $k/s \approx 0.38$, and brown (● ● ●) for trapezoidal riblets with smaller k/s. All riblets have similar tip angles, ranging from 54° to 60°. For the numerical cases, different triangle orientations correspond to different l_g values: ◀ for $l_g = 0.053$, ▲ for $l_g = 0.12$ and ▼ for $l_g = 0.24$. Of the present DNS results, green markers (▲) correspond to values of ΔU^+ calculated directly from the mean velocity profiles, while for the white markers (△) the value is calculated from the friction coefficients, as per Equation 4.8 from Gatti and Quadrio [6], in accordance with the experiments. The dashed line represents the fully rough regime from Perry et al. [13].

The cases at $l_g^+ = 20, 30, 50$ align well with the k-roughness predictions from Perry et al. [13], who estimated $\Delta U^+ = \mathtt{k}^{-1} log(l_g^+) + B$, with constants $\mathtt{k} = 0.39$, $B = -7.3$. It remains unclear why geometries that are insensitive to pressure drag should nonetheless exhibit the characteristic behavior of pressure-drag-dominated rough surfaces over a specific range of l_g^+.

Figure 2 shows the passive scalar roughness function as a function of the riblets' viscous size. A trend similar to that of friction is observed: cases with $l_g^+ \leq 50$ appear to follow the fully rough asymptote, whereas for larger geometries the riblet friction behavior becomes independent of viscous size. In this case, good agreement between the $\Delta\Theta^+$ values obtained from the Stanton number and those obtained from the mean profiles is observed.

Some observations shall be made regarding the flow behavior in the outer layer. While for drag-reducing riblets the wall geometry acts as a wall-normal shift of the mean flow and turbulence, as riblets' effect can be modelled as an simple increase of the viscous sublayer thickness, in the present cases turbulence can hardly be considered as smooth-wall-like. In particular, for some configurations, especially those with larger riblets, we observe a partial loss of outer-layer similarity, despite the domain dimensions being sufficiently large to avoid minimal-channel-like effects [9]. It is known for smooth walls that the mismatch between mean velocity and scalar profiles grows with Reynolds number [1]; here the ribbed walls appear to amplify that mismatch, most noticeably in the outer layer. Whether this behaviour is caused by the large riblet size relative to the channel remains unclear. The outer-layer dynamics are ultimately dictated by the case geometry, which here is significantly modified with respect to a smooth channel. Nevertheless, comparisons of C_f and C_h for different outer-unit sizes at the same l_g^+ show only minimal differences, suggesting that the l_g value has little influence on the global statistics.

Reynolds analogy data in Figure 3 indicate that all eight cases lie slightly on the favourable side, with $l_g^+ = 50$, 100 geometries improving the Reynolds analogy factor by approximately 2%. The Reynolds analogy coefficient is calculated as $RA = 2C_h/C_f$, and is compared to that of a smooth channel (RA_0).

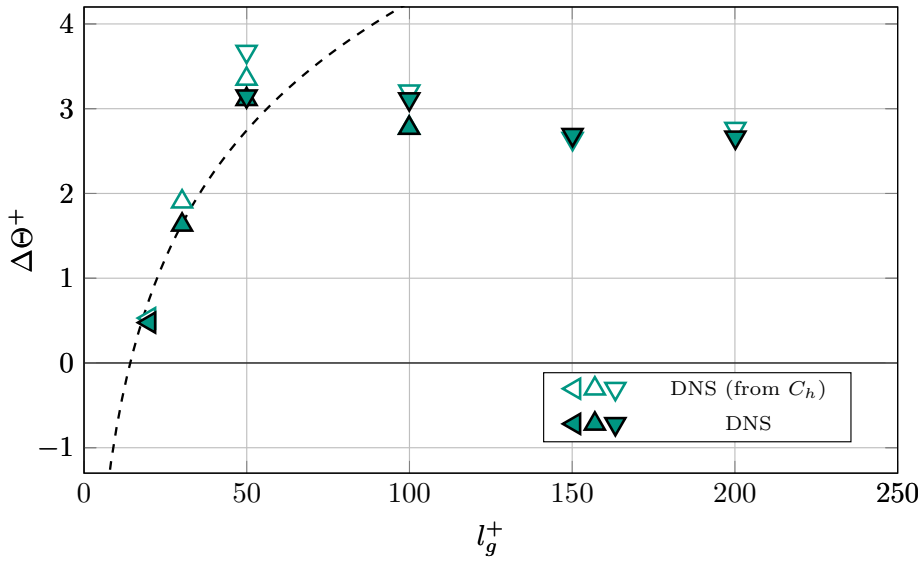

Figure 2: Temperature roughness functions for the simulated riblet cases. White markers (△) correspond to values of $\Delta\Theta^+$ calculated directly from the mean temperature profiles, while for the green markers (▲) the value is calculated from the Stanton numbers. The dashed line represents the fully rough regime.

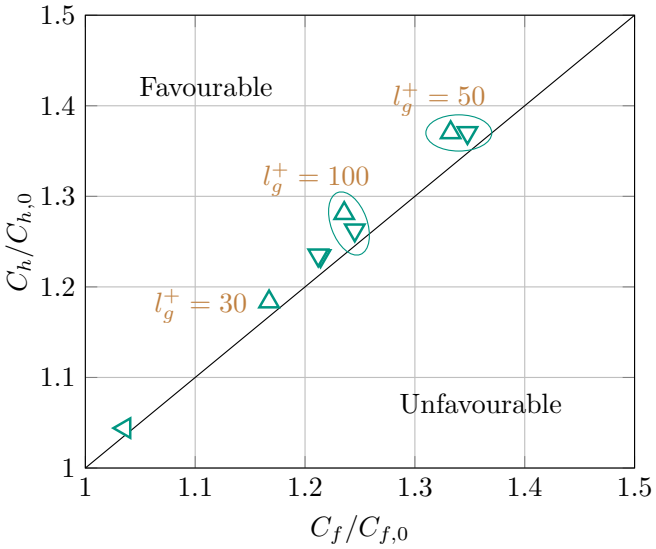

Figure 3: Plot comparing the Reynolds analogy factor of ribbed cases with their smooth reference counterparts. Points in the upper-left region indicate that the ratio $C_h/C_{h,0}$ exceeds $C_f/C_{f,0}$, signifying that heat transfer is enhanced more than momentum transfer, resulting in a favourable Reynolds analogy breaking. On the other hand, points in the lower-right region indicate the opposite.

In this case the friction coefficient and Stanton number are calculated via a simple integration of the mean velocity and temperature profiles. In general, it seems that structures which impact the most the momentum and heat exchange with respect to smooth surfaces are the ones more likely to break favourably the Reynolds analogy for this kind of geometries.
The focus is now on understanding which physical phenomena can be retained responsible for this increase in thermal efficiency. It was shown by Rouhi et al. [15] that the rise of Kelvin Helmholtz rollers can be

associated to a positive effect in the Reynolds analogy factor, while turbulent secondary motions have an opposite effect. Yet, in these cases large spanwise rollers are present to some extent, but definitely not as much as for sawtooth or blade riblets, and the breaking of the Reynolds analogy in these cases seems more linked to discrepancies in the outer layer between the velocity and scalar profiles.

4 Conclusions and Developments

We presented results on friction and heat transfer for ribbed channel flows, confirming that these geometries deviate from the typical k-roughness regime due to their streamwise alignment. Results are confirmed both when the roughness function ΔU^+ is calculated from the friction coefficient and when it is calculated from the mean velocity profile. Further investigations are underway to show that this behavior is linked to turbulence perceiving the ribbed walls as piecewise smooth, and the lack of pressure drag suggests that these surfaces should behave differently from a typical k-roughness regime. On the other hand, it remains unclear why for a certain range of l_g^+ riblets actually follow the behavior typical of classical rough surfaces. Results also suggest a slight enhancement in thermal efficiency for the current geometry. Further analysis will provide a measure of the impact of secondary flows and spanwise rollers on heat and momentum transfer, and an innovative framework for assessing the Reynolds analogy factor based on momentum and scalar dissipation.

References

[1] Abe, H. and Antonia, R. A. Relationship between the heat transfer law and the scalar dissipation function in a turbulent channel flow. *Journal of Fluid Mechanics*, 830:300–325, November 2017. ISSN 0022-1120, 1469-7645. doi: 10.1017/jfm.2017.564.

[2] Bechert, D., Bruse, M., Hage, W., Hoeven, J. V. D., and Hoppe, G. Experiments on drag-reducing surfaces and their optimization with an adjustable geometry. *Journal of Fluid Mechanics*, 338:59–87, 1997.

[3] Endrikat, S., Modesti, D., MacDonald, M., García-Mayoral, R., Hutchins, N., and Chung, D. Direct Numerical Simulations of Turbulent Flow Over Various Riblet Shapes in Minimal-Span Channels. *Flow, Turbulence and Combustion*, 107(1):1–29, June 2021. ISSN 1573-1987. doi: 10.1007/s10494-020-00224-z.

[4] Garcia-Mayoral, R. and Jiménez, J. Hydrodynamic stability and the breakdown of the viscous regime over riblets. *Journal of Fluid Mechanics*, 678:317–347, 2011. doi: 10.1017/jfm.2011.114.

[5] García-Mayoral, R. and Jiménez, J. Drag reduction by riblets. *Philosophical Transactions of the Royal Society A*, 369(1940):1412–1427, 2011.

[6] Gatti, D. and Quadrio, M. Reynolds-number dependence of turbulent skin-friction drag reduction induced by spanwise forcing. *Journal of Fluid Mechanics*, 802:553–58, 2016.

[7] Gatti, D., Cipelli, S., Gattere, F., Chiarini, A., Luchini, P., and Quadrio, M. Accurate and efficient Direct Numerical SImulation of drag reduction with riblets. In *Euromech Turbulence Conference (ETC18)*, Valencia (Spain), 2023.

[8] Ibrahim, J. I., Gomez-de-Segura, G., Chung, D., and Garcia-Mayoral, R. The smooth-wall-like behaviour of turbulence over drag-altering surfaces: A unifying virtual-origin framework. *Journal of Fluid Mechanics*, 915:A56, 2021. ISSN 0022-1120. doi: 10.1017/jfm.2021.13.

[9] Lozano-Durán, A. and Jiménez, J. Effect of the computational domain on direct simulations of turbulent channels up to $\mathrm{Re}_{\backslash \mathrm{tau}} = 4200$. *Physics of Fluids*, 26:011702 1–7, 2014.

[10] Luchini, P. A deferred correction multigrid algorithm based on a new smoother for the Navier–Stokes equations. *Journal of Computational Physics*, 92:349–368, 1991.

[11] Luchini, P., Gatti, D., Chiarini, A., Gattere, F., Atzori, M., and Quadrio, M. A simple and efficient second-order immersed-boundary method for the incompressible Navier–Stokes equations. *Journal of Computational Physics*, 539:114245, 2025. doi: 10.1016/j.jcp.2025.114245.

[12] Modesti, D., Endrikat, S., Hutchins, N., and Chung, D. Dispersive stresses in turbulent flow over riblets. *Journal of Fluid Mechanics*, 917:A55, June 2021. ISSN 0022-1120, 1469-7645. doi: 10.1017/jfm.2021.310.

[13] Perry, A., Schofield, W., and Joubert, P. Rough wall turbulent boundary layers. *Journal of Fluid Mechanics*, 37:383–413, 1969.

[14] Pirozzoli, S. and Orlandi, P. Natural grid stretching for DNS of wall-bounded flows. *Journal of Computational Physics*, 439:110408, August 2021. ISSN 0021-9991. doi: 10.1016/j.jcp.2021.110408.

[15] Rouhi, A., Endrikat, S., Modesti, D., Sandberg, R. D., Oda, T., Tanimoto, K., Hutchins, N., and Chung, D. Riblet-generated flow mechanisms that lead to local breaking of Reynolds analogy. *Journal of Fluid Mechanics*, 951:A45, November 2022. ISSN 0022-1120, 1469-7645. doi: 10.1017/jfm.2022.880.

[16] Rowin, W. A., Deshpande, R., Wang, S., Kozul, M., Chung, D., Sandberg, R. D., and Hutchins, N. Experimental characterisation of Kelvin–Helmholtz rollers over riblet surfaces. *Journal of Fluid Mechanics*, 1009:A65, April 2025. ISSN 0022-1120, 1469-7645. doi: 10.1017/jfm.2025.306.

[17] von Deyn, L. H., Gatti, D., and Frohnapfel, B. From drag-reducing riblets to drag-increasing ridges. *J Fluid Mechanics*, 951:A16, November 2022. ISSN 0022-1120, 1469-7645. doi: 10.1017/jfm.2022.796.